

# Modification of Nanoporous Silicon Nitride with Stable and Functional Organic Monolayers

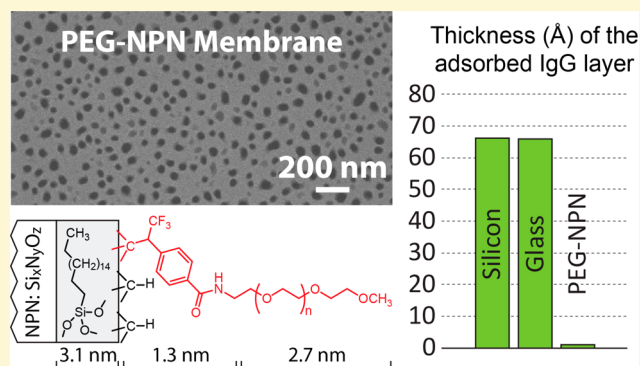
Xunzhi Li,<sup>†</sup> Dean Johnson,<sup>‡</sup> Wenchuan Ma,<sup>†</sup> Henry Chung,<sup>‡</sup> Jirachai Getprechawsawas,<sup>‡</sup> James L. McGrath,<sup>\*,‡</sup> and Alexander A. Shestopalov<sup>\*,†</sup>

<sup>†</sup>Department of Chemical Engineering, University of Rochester, Rochester, New York 14627, United States

<sup>‡</sup>Department of Biomedical Engineering, University of Rochester, Rochester, New York 14627, United States

**S** Supporting Information

**ABSTRACT:** This study describes the formation of functional organic monolayers on thin, nanoporous silicon nitride membranes. We demonstrate that the vapor-phase carbene insertion into the surface C–H bonds can be used to form sub-5 nm molecular coatings on nanoporous materials, which can be further modified with monolayers of polyethylene glycol (PEG) molecules. We investigate composition, thickness, and stability of the functionalized monolayers and the changes in the membrane permeability and pore size distribution. We show that, due to the low coating thickness (~7 nm), the functionalized membrane retains 80% of the original gas permeance and 40% of the original hydraulic permeability. We also show that the carbene/PEG functionalization is hydrolytically stable for up to 48 h of exposure to water and that it can suppress nonspecific adsorption of the proteins BSA and IgG. Our results suggest that the vapor-phase carbenylation can be used as a complementary technology to the traditional self-assembly and polymer brush chemistries in chemical functionalization of nanoporous materials, which are limited in their ability to serve as stable coatings that do not occlude nanomembrane pores.



## INTRODUCTION

Ultrathin and porous silicon membranes (nanomembranes) are finding increasing utility as highly manufacturable and highly permeable components for biological separations,<sup>1–4</sup> cell culture,<sup>5,6</sup> micropumps,<sup>7,8</sup> and sensors.<sup>9</sup> The ability to stably coat nanomembranes with organic films without closing pores or reducing permeability would dramatically expand the diversity of functions and enhance performance in each of these applications. For example, the ability to reduce or eliminate biomolecular adsorption would improve biocompatibility in applications such as hemodialysis.<sup>2</sup> Electroosmotic micropumps are likely to perform more efficiently if a high density of surface charge<sup>3</sup> were provided by branched ionic oligomers grafted to the membrane surface. Affinity encoded, surface-grafted peptides or other organic molecules could improve the specificity of membranes used in sensors of biological or hazardous molecules. We recently introduced ultrathin nanoporous silicon nitride (NPN)<sup>10</sup> as a more mechanically robust, more chemically stable, and lower-cost alternative to the original nanomembrane material made from pure silicon.<sup>11</sup> Our objective in this work is to develop a general strategy for the coating of NPN with stable organic molecules that add functionality without diminishing the benefits of high permeability and size selectivity of the nanomembranes.

Nanomembranes impose several restrictions on the properties of organic coatings that can be used to modify their

interfaces: (1) to effectively modulate membrane's chemical and physical properties, the coating must accept a wide variety of organic functionalities; (2) the thickness of the coating should be controlled and limited to the pore radius (1–10 nm) to have a predictable effect on the pore size; (3) the coating should be stable in typical hydrolytic environments; (4) the deposition conditions must ensure that the pore interface is coated with the moieties required for a specific membrane function and not damaged during the processing. Such requirements mean that the traditional polymer brushes (PBs) and self-assembled monolayers (SAMs) have limitations for the modification of nanomembranes with stable and functional organic groups: traditional PB approaches do not provide a robust mechanism to control PB thickness down to 1–10 nm, and the majority of PBs thinner than 15 nm suffer from poor hydrolytic stability,<sup>12–17</sup> while SAMs on nanostructured or rough surfaces have disrupted two-dimensional van der Waals (vdW) interactions and disordered organic phases that lead to monolayer defects and decreased stability.<sup>18–23</sup> Moreover, the SAM approach requires small centrosymmetric molecules that can participate in self-assembly, limiting the variety of organic functionalities.<sup>24–27</sup>

Received: December 20, 2016

Revised: February 20, 2017

Published: February 22, 2017

A different technique that avoids some of the PB and SAM limitations relies on organic monolayers that are attached to the membranes via thermodynamically stable, nonhydrolytic surface bonds (e.g., nonpolar C–C or Si–C bonds). Such monolayers (1) do not rely on self-assembly for stability, (2) can utilize noncentrosymmetric molecules with more diverse functionalities, and (3) have a small effect on the geometry of nanostructured features because their size is limited to several nanometers. However, the majority of the grafting reactions that attach organic molecules to inorganic materials via stable C–C and Si–C bonds have high activation energies and require aggressive reactive environments that can be damaging to ultrathin, nanoporous substrates.<sup>28–44</sup>

Recently, we reported formation of stable and functional organic monolayers on hard and soft interfaces via a vapor-phase carbene insertion into Si–H and C–H bonds.<sup>45</sup> We demonstrated that functional carbene precursors can be used to form uniform, monomolecular coatings on silicon, silicon nitride, and urethane-acrylate polymers under mild vacuum conditions and exposure to UV light. The reported method attaches functional carbenes via stable and nonhydrolytic Si–C and C–C bonds, achieving high molecular coverage and good long-term stability in air, isopropanol, and water without relying on self-assembly. The overall thickness of these monolayers was limited to ~1.3 nm. One of the important features of the reported method is a vapor-phase deposition that permits facile functionalization of polymeric soft materials that are easily damaged by solution-phase processing. Solution-phase deposition of carbenes on nanomembranes is also complicated due to the undesired capillary effects, poor carbene precursor solubility, incomplete pore filling, and material contamination and crystallization during drying. In addition, vapor-phase deposition has the potential for simple large-area functionalization of porous, bulky, or air-sensitive materials and the prospect of utilizing the same or similar equipment with physical vapor or molecular layer depositions.

Here, we report functionalization of ultrathin nanoporous silicon nitride membranes with stable and functional organic molecules via the carbene insertion chemistry. The described coating comprises a thin, inert polymer layer that serves as the attachment interface for the carbene molecules and a stable polyethylene glycol (PEG) terminated organic monolayer that is linked to the polymer via nonhydrolytic C–C bonds generated by the vapor-phase carbene insertion. We confirm the overall structure of the coating and investigate its thickness, stability, and antifouling performance. We demonstrate that the proposed strategy can be used to effectively modify nanoporous silicon nitride with the desired organic functionalities without significantly impacting its pore-size distribution or transport properties.

## MATERIALS AND METHODS

**Materials.** Porous silicon nitride membranes (NPN) were purchased from SiMPore Inc. (West Henrietta, NY). Figure S1 shows the general structure and dimension of the NPN chips. The average size and aspect ratio of the NPN pores are 50.7 nm and ~1:1. The pores are uniformly distributed over the entire chip area with ~120  $\mu\text{m}^2$  density. The XPS spectrum of NPN was used to calculate its bulk composition (Figure S2 and Table S1). XPS analysis revealed that the untreated NPN chips have a thin layer of perfluorinated carbon material that probably accumulates on the silicon nitride surface during the reactive ion etching (one of the processing steps in making NPN<sup>10</sup>).

Our approach to stable organic monolayers relies on the ability of functional carbene precursors to generate active carbenes in the presence of UV light and their ability to form stable, nonhydrolytic C–C bonds upon the insertion into the surface C–H bonds. As a carbene precursor, we used 2,5-dioxopyrrolidin-1-yl 4-(3-(trifluoromethyl)-3H-diazirin-3-yl)benzoate (NHS-diazirine, Figure S3). This molecule releases diatomic nitrogen and generates reactive carbene species when exposed to UV light. The generated carbenes can react with the surface Si–H and C–H groups leading to the chemical immobilization of the NHS moieties through the stable Si–C and C–C bonds. NHS-diazirine was synthesized in 10 steps following the previously published protocol.<sup>45</sup> To generate a C–H terminated inert coating on NPN that can accept carbene molecules, we first installed and annealed a thin alkyl-silane layer. As such, NPN chips were oxidized in oxygen plasma and exposed to the 10:1 (v/v) mixture of octyl triethoxysilane (OTC) and trimethylamine vapor overnight at mild vacuum at 75 °C. The resulting substrates were rinsed with isopropanol and annealed at 110 °C at the reduced pressure to produce NPN chips coated with thin methylated films (Me-NPN). We note that this layer is different in structure and thickness from the corresponding OTS self-assembled monolayers on silicon nitride and silicon oxide. Our silane coating resembles a multilayered polymeric film and is therefore less prone to hydrolytic degradation than typical silane SAMs.

**Chemical Functionalization of NPN with PEG Molecules.** *NHS-Terminated NHS-NPN Substrates.* The vapor-phase deposition of NHS-diazirine was conducted in a glass vacuum chamber at 200 mTorr of pressure. The Me-NPN substrates were positioned 10 cm away from the source containing 7.5 mg of NHS-diazirine. The source was heated to melt the NHS-diazirine (~130 °C), and the UV light was introduced from the sides of the vacuum chamber to generate the carbenes and enable the monolayer formation. After 90 min, the NHS-functionalized substrates (NHS-NPN) were rinsed with isopropanol and dichloromethane to remove physisorbed molecules and dried with filtered nitrogen.

*PEG-Terminated PEG-NPN Substrates.* To install polyethylene glycol (PEG) groups, NHS-NPN chips were reacted with the 10 mM solution of PEG<sub>1000</sub>-NH<sub>2</sub> molecule in a 10:1 (v/v) isopropanol/triethylamine mixture for 12 h at 23 °C. Following the reaction, the chips were rinsed with isopropanol and dried under filtered nitrogen (PEG-NPN substrates).

**XPS Measurements.** XPS spectra were recorded on the Kratos Axis Ultra DLD XPS spectrometer equipped with a mono-Al X-ray source (1468.6 eV). The XPS spectra were collected using the widest lens and largest aperture analyzer settings (~600 × 900  $\mu\text{m}$  substrate area). Multiple sweeps were recorded for the survey and regional scans (typically 7–10 sweeps) to increase signal-to-noise ratio. Unless specified, the electron collection angle  $\Theta$  in all XPS measurements was zero. The XPS signal areas were measured using Casa XPS software.

*Electron Attenuation Length.* The values for the attenuated length of F 1s, C 1s, and Si 2p electrons in the monolayer were calculated using NIST Electron Effective-Attenuation-Length Database: F 1s,  $\lambda = 25.17$  Å; C 1s,  $\lambda = 34.52$  Å; Si 2p,  $\lambda = 38.62$  Å.<sup>46</sup>

*Coating Thickness.* Regional C 1s, F 1s, and N 1s spectra of the Me-NPN, NHS-NPN, and PEG-NPN were used to measure the thicknesses of the methylated silane film and NHS- and PEG-terminated monolayers. We calculated the thickness of each layer by analyzing distinctive film and substrate XPS signals after each reaction.<sup>47–49</sup> In short, this analysis accounts for the influence of the film thickness on the intensity of the photoemission from the underlying substrate. We used eq 1 that relates total XPS intensities  $I_{A(f)}$  and  $I_{B(s)}$  of the characteristic film (A) and substrate (B) atoms in the case of a homogeneous film (f) of the thickness “d” on the substrate(s) (see Table S1 for more details):

$$\frac{I'_{A(f)}}{I'_{B(s)}} = \frac{N_{A(f)}}{N_{B(s)}} \times \frac{1 - \exp(-d/\lambda_{A(f)} \times \cos \theta)}{\exp(-d/\lambda_{B(f)} \times \cos \theta)} \quad (1)$$

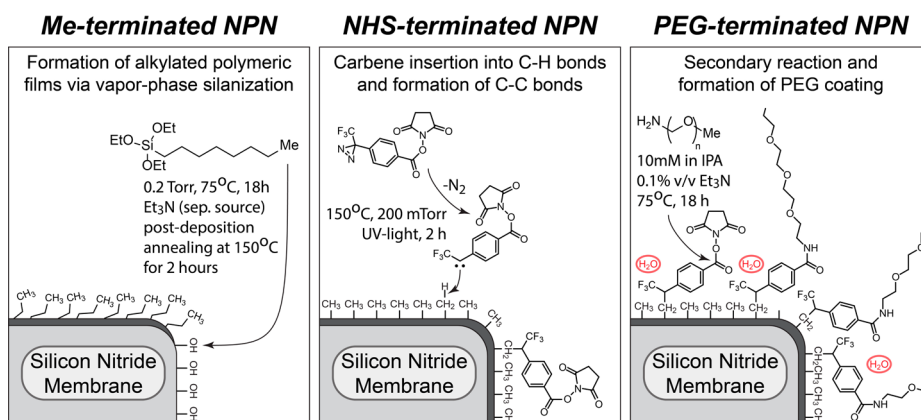


**Figure 1.** Chemical functionalization of NPN membrane with PEG molecules.

$$\frac{I'_{A(f)}}{I'_{B(s)}} = \frac{I_{A(f)} \times \lambda_{B(f)} \times \text{RSF}_B}{I_{B(s)} \times \lambda_{A(f)} \times \text{RSF}_A}, \quad \frac{N_{A(f)}}{N_{B(s)}} = \frac{\rho_f \times X_{A(f)} \times M_s}{\rho_s \times X_{B(s)} \times M_f}$$

where  $I'_{A(f)}$ : correlated area intensity of the element A in the film;  $I'_{B(s)}$ : correlated area intensity of the element B in the substrate;  $I_{A(f)}$ : area intensity of the element A in the film;  $I_{B(s)}$ : area intensity of the element B in the substrate;  $N_{A(f)}$ : atomic density of the element A in the film;  $N_{B(s)}$ : atomic density of the element B in the substrate;  $d$ : film thickness;  $\lambda_{A(f)}$ : inelastic mean free path (the attenuated length) of the electrons A in the film;  $\lambda_{B(f)}$ : inelastic mean free path (the attenuated length) of the electrons B in the film;  $\theta$ : the emission angle of the electrons with respect to the surface normal;  $\text{RSF}_A$ : atomic sensitivity factor of element A;  $\text{RSF}_B$ : atomic sensitivity factor of element B;  $\rho_f$ : film density;  $\rho_s$ : substrate density;  $M_f$ : film molecular weight;  $M_s$ : substrate molecular weight;  $X_{A(f)}$ : stoichiometric number of the element A in the film;  $X_{B(s)}$ : stoichiometric number of the element B in the substrate.

**NPN Hydrolytic Stability.** We tested hydrolytic stability (up to 48 h of exposure) of the Me-NPN, NHS-NPN, and PEG-NPN membranes at room temperature in air, isopropanol, water (pH = 7.0), and PBS buffer (pH = 7.4). These conditions represent typical environments to which membranes are subjected when stored and used. The stability was measured by monitoring changes in the normalized C 1s and F 1s XPS peak areas, which correspond to the changes in the coating density (C 1s and F 1s signals are indigenous to the coating layers and are not present in the bulk NPN). For each exposure condition, a single chip was used to provide 1 min and 48 h data points for the stability plots to ensure that the observed differences do not originate from the changes in the processing conditions. To reduce errors associated with the drift in the XPS count intensity over time or due to the differences in the sample focus position, the XPS areas of the monolayer signals were normalized with the respect to the indigenous Si 2p substrates signal.

**NPN Transport and Permeability.** We investigated the impact of PEG functionalization on nanomembrane performance through gas and water permeance measurements and membrane sieving characteristics before and after functionalization.

**Gas Permeance.** Gas permeance was measured with nitrogen gas as previously described.<sup>9,10</sup> Briefly, a NPN chip was housed in a custom-made microcentrifuge tube with a snap-on holder at the bottom. The holder part of the tube was designed to secure the chip between two silicone gaskets and allowed the flow-through to exit via slits at the bottom. The top opening of the tube was made accessible to standard tubing. Once assembled, the tube was connected to the N<sub>2</sub> source where the gas flow rate and pressure were monitored by an OMEGA rotameter (FL-3803ST) and VWR digital manometer (VWR 33500-084), respectively. Five data points of the gas flow rates at various applied pressures (0.3–1 PSI) were collected for each membrane; five NPN and five PEG-NPN chips were tested. All chips had an active membrane area of 0.015 cm<sup>2</sup>. The permeance was found by dividing

the slope of the volumetric flow rate vs pressure graph by the active membrane area.

**Hydraulic Permeability.** The flow rate of deionized (DI) water transported across each membrane was measured as previously described.<sup>1,10</sup> To measure the flow rate, the chip was clamped between two o-rings and housed in a two-halves fluidic chamber of a leak-proof pressurized system. The volumetric flow rate was calculated from the displacement of a liquid meniscus traveling in the tubing that connected the fluidic chamber to an air-pressure regulator (Marsh Bellofram). Nine data points of the liquid flow rates at various applied pressures were collected for each membrane; seven NPN and three PEG-NPN chips were tested. The hydrostatic permeability was determined from the average ratio of the volumetric flow rate to the applied pressure per membrane active area.

**Sieving Coefficients.** The sieving behavior of each membrane was examined from the transport of gold-nanoparticle (NP) ladder as previously described.<sup>1,10</sup> Similar to the N<sub>2</sub> permeance measurements, a custom-made microcentrifuge tube was used to hold each chip. An aqueous solution of Au nanoparticles (BBI Solutions) of uniform size was filtered through the membrane, and the filtrate was analyzed by UV absorption to determine the amount of Au nanoparticles passing through. Various sizes of Au nanoparticles were used to obtain the sieving curve for each type of membrane; each chip was used only once to avoid cross-contamination. In each experiment, 100  $\mu$ L of stock gold NPs was added to 300  $\mu$ L of ultrapure water. 300  $\mu$ L of this mixture was added to the microcentrifuge tube and held at 1.3 PSI until 100  $\mu$ L passed to the filtrate.

**Protein Adsorption.** The ability of the PEG-NPN chips to limit nonspecific protein adsorption was assessed by exposing PEG-NPN and other control substrates to the BSA and IgG solution. Here, after a prewetting rinse with PBS (60 s), the chips were incubated with 1 mg/mL BSA or IgG proteins dissolved in PBS solution (pH = 7.4) in a humidified chamber for 2 h at 4 °C. The samples were rinsed with PBS and then DI water (60 s) and dried with filtered compressed air. The exposed chips were analyzed by XPS to determine the thickness of the adsorbed protein layer.

## RESULTS AND DISCUSSION

**Chemical Functionalization of NPN Membranes.** We have previously demonstrated that NHS-diazirine can directly react with the H-terminated silicon nitride to form dense monolayers that have good hydrolytic stability for up to 2 weeks in air, isopropanol, and water.<sup>45</sup> However, nanoporous NPN has a substantial amount of oxygen atoms that can promote carbene insertion into the surface O–H bonds leading to the hydrolytic O–C attachment. To avoid unstable bonding, we passivated NPN substrates with an ultrathin methylated alkyl silane film that provides necessary C–H bonds for the carbene attachment and acts as a chemically inert passivating

barrier to more reactive NPN (Me-NPN, Figure 1). Subsequent vapor-phase deposition of NHS-diazirine was conducted in a glass vacuum chamber under UV light illumination to promote carbene formation and insertion into the C–H bonds of the aliphatic silane film (NHS-NPN, Figure 1). To install polyethylene glycol groups, NHS-NPN chips were reacted with the monosubstituted amino PEG molecule (PEG<sub>1000</sub>-NH<sub>2</sub>, average  $M_n = 1000$ ) in isopropanol (PEG-NPN, Figure 1).

Me-NPN, NHS-NPN, and PEG-NPN chips were analyzed by X-ray photoelectron spectroscopy (XPS), water contact angle goniometry, and scanning electron microscopy (SEM) to determine the structure and composition of the deposited layers and changes in the membrane pore size distribution. Figure 2 shows regional F 1s and C 1s XPS spectra of the Me-

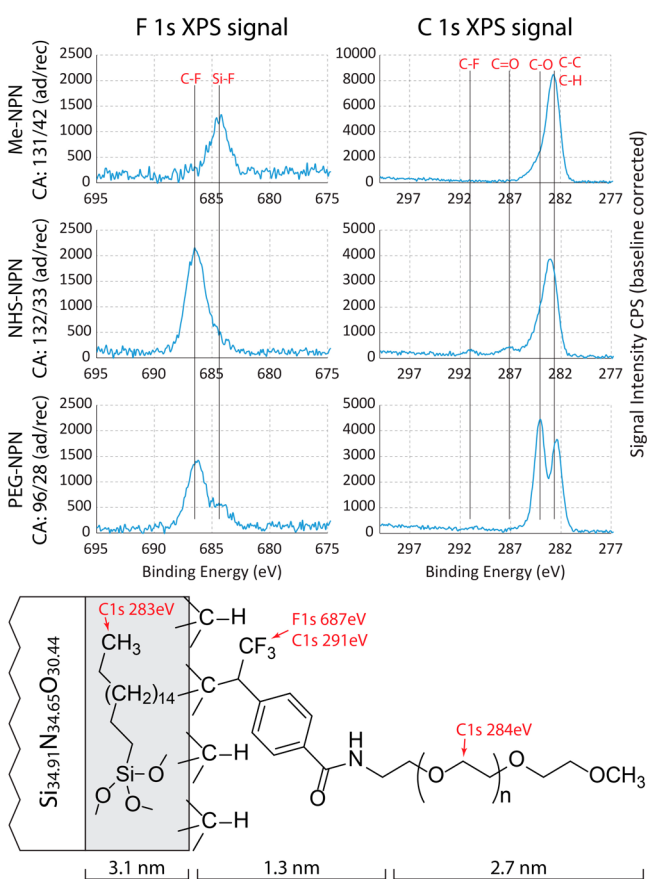


**Figure 2.** Regional XPS spectra and advancing/receding water contact angles of the silane, NHS-diazirine, and PEG layers (top); chemical structure and dimensions of the PEG-NPN substrate (bottom).

NPN, NHS-NPN, and PEG-NPN substrates that verify successful functionalization of NPN. The XPS regional scan of the methylated Me-NPN substrate contains a characteristic C 1s peak at 283–284 eV that corresponds to the mixture of C–H and C–O bonds in the silane coating. The subsequent carbene insertion results in the additional C–F and C=O peaks at 291 and 287 eV in the regional C 1s XPS spectrum of the NHS-NPN substrate. The final reaction with the PEG molecule increases the intensity of the C–O peak at 284 eV in the C 1s XPS spectrum of the PEG-NPN substrate. The F 1s spectrum of Me-NPN has a small signal at 684 eV which is associated with the fluorine-based reactive ion etching during the NPN processing. F 1s XPS spectra of NHS-NPN and PEG-NPN have additional F 1s peaks at 687 eV from the NHS-

diazirine molecule that contain three C–F bonds. The advancing and receding water contact angles of the Me-NPN, NHS-NPN, and PEG-NPN substrates decrease from a hydrophobic silane coating to a more hydrophilic PEG layer (Figure 2). The large contact angle hysteresis on all three substrates is likely attributed to the porous nature of NPN.

The measured thicknesses of the methylated silane coating (3.1 nm), NHS-terminated monolayer (1.3 nm), and PEG-functionalized monolayer (2.7 nm) are in a good agreement with the proposed structure of the PEG-NPN substrate (Figure 2, bottom). These measurements suggest that the initial reaction of the NPN chip with the OTC molecule produces a thin multilayered film, whereas the subsequent reactions with the NHS-diazirine and PEG<sub>1000</sub>-NH<sub>2</sub> form monolayers. These findings are in agreement with our previous measurements of thicknesses of the NHS-diazirine monolayers on various flat substrates,<sup>45</sup> and they confirm that the vapor-based carbene insertion can be applied to functionalize nanoporous materials.

Subsequently, we imaged NPN, Me-NPN, NHS-NPN, and PEG-NPN membranes using SEM to determine the changes in the pore size distribution. Figure 3 shows SEM images of the

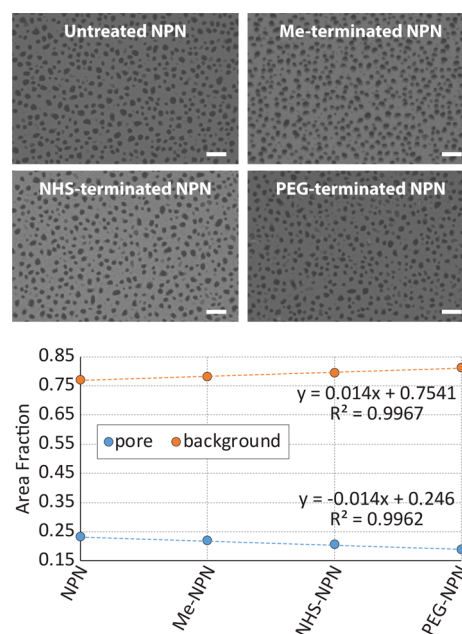


**Figure 3.** SEM images (top) and pore-to-background surface area ratio (bottom) of the untreated and modified NPN membranes. Scale bar is 200 nm.

untreated and functionalized substrates and their pore-to-background surface area ratios (calculated from the monochromatic histograms of the corresponding SEM images; see Figure S4 for more details). SEM analysis shows that the pore size gradually decreases from the untreated substrate to the PEG-modified sample in the order which is consistent with the proposed PEG-pSiN structure and functionalization sequence (NPN > Me-NPN > NHS-NPN > PEG-NPN). Together, XPS and SEM data show that the described protocol can modify nanoporous silicon nitride with the functional PEG molecules without blocking the pores.

**Hydrolytic Stability of PEG-Modified NPN Membranes.** The stability of the functionalized membranes was plotted as normalized XPS peak areas of the C 1s and F 1s signals (Figure 4 and Table S2). Our measurements show that

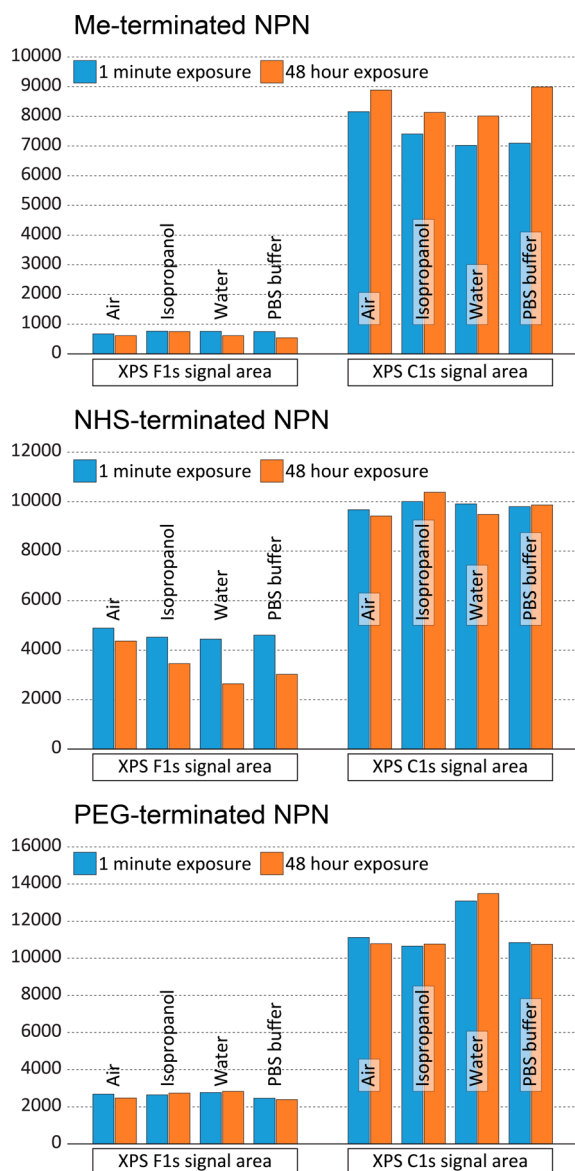


**Figure 4.** Normalized F 1s and C 1s XPS peak areas of the Me-NPN (top), NHS-NPN (middle), and PEG-NPN (bottom) membranes after 1 min (blue) and 48 h (orange) of exposure to air, isopropanol, water, and PBS buffer.

the inert silane coating (Me-NPN) has good hydrolytic stability in all environments; however, due to its hydrophobic nature, it readily physisorbs organic materials, which is evident from the increase in the C 1s peak areas after 48 h of exposure in all tested conditions. NHS-terminated substrate (NHS-NPN) demonstrates good stability in nonaqueous environments, which is evident by a small decrease in the F 1s XPS peak area after the exposure to air and isopropanol, and adequate stability in water and PBS buffer (~35% decrease in the F 1s XPS peak intensity). The drop in the F 1s XPS peak intensity of the NHS-NPN substrate can also be associated with the hydrolysis of the charge-neutral NHS groups, which is accelerated in water, and subsequent charging of the resulting  $-\text{COOH}$  groups during the XPS analysis. The presence of the charged species can distort XPS measurements due to the nonproportional changes in the inelastic mean free path of the X-ray generated substrate and film electrons.<sup>50</sup> The hypothesis that the measured drop in the F 1s peak area of the NHS-NPN

substrate upon exposure to water and PBS is related to the NHS hydrolysis and surface charging is also supported by the stability measurements of the PEG-NPN substrate. The PEG-terminated system replaces hydrolytic NHS esters with stable amide bonds, resulting in a charge-neutral interface. The PEG-terminated substrate demonstrates excellent stability in all environments without significant changes in its F 1s or C 1s signal areas. PEG-terminated coatings are known to suppress nonspecific adsorption of organic and biological molecules, which is corroborated by very small changes in the C 1s peak areas upon exposure to air, isopropanol, water, and PBS. These measurements show that the developed PEG coating, despite its overall low thickness and the lack of self-assembled organic phases, demonstrates good hydrolytic stability even on nanoporous materials, where the traditional SAM-based approaches have limitations due to geometrically constrained vdW ordering.<sup>51–53</sup>

**Permeability and Sieving Section.** We next examined the impact of PEG coatings on the separation and transport characteristics of NPN. Following well-established procedures in our lab,<sup>1,10</sup> we measured the transmission of monodisperse gold nanoparticles of different sizes under constant pressure to create “sieving curves” for both coated and uncoated membranes. Results show that NPN and PEG-NPN sieving curves have similar shapes but with a shift in the cutoff from ~50 to ~36 nm (Figure 5A). This reduction is consistent with

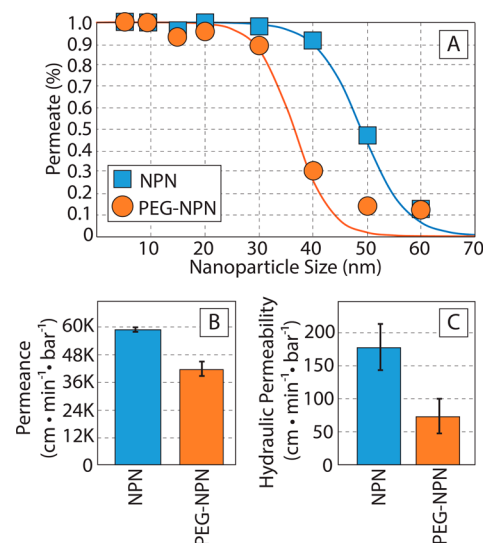


**Figure 5.** Impact of PEG functionalization on NPN transport properties. (A) Sieving curves obtained using a gold nanoparticles size ladder. (B) Gas permeance values measured from the normalized flow rate of  $\text{N}_2$  under constant pressure. (C) Hydraulic permeability values measured from the normalized flow rate of deionized water under constant pressure.

the combined thickness (7 nm) of the silane, NHS, and PEG layers shrinking pores in an axisymmetric fashion to give a total reduction of 14 nm. These data provide compelling evidence that our PEG coating strategy conformally coats pore walls.

Again, following well-established methods from our lab,<sup>1,9,10</sup> we examined the impact of PEG coating on the permeance of NPN to gas and water flow (hydraulic permeability). As expected, both values are affected by the constriction of pores (Figure 5B,C), but hydraulic permeability is more strongly affected. This result can be partly understood from the fact that

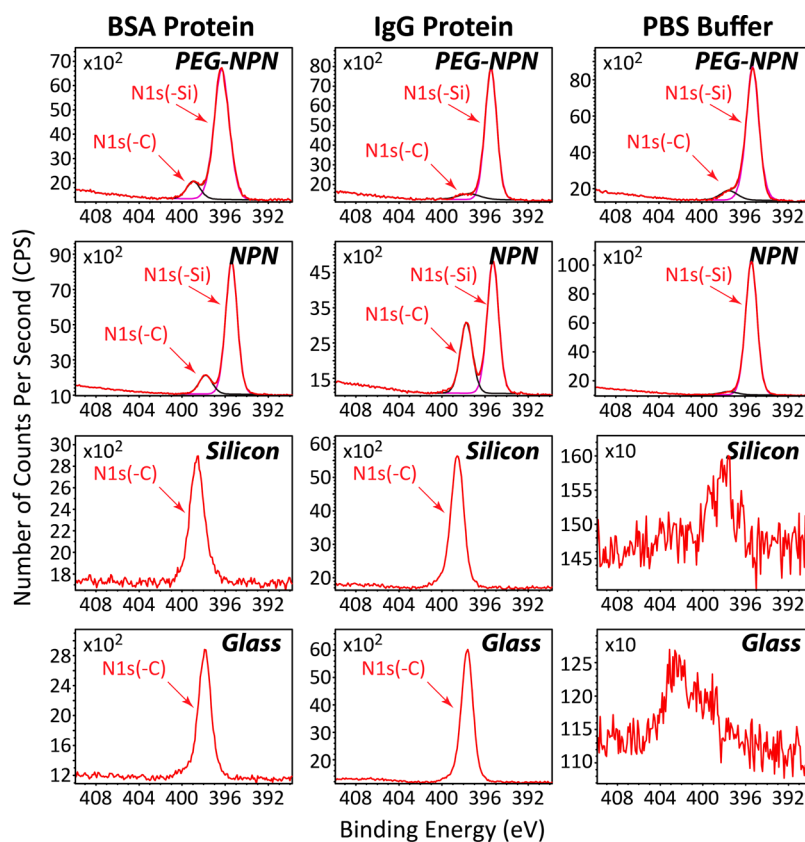


**Figure 6.** Regional N 1s XPS spectra of the PEG-NPN, NPN, silicon, and glass substrates exposed to the BSA and IgG protein solutions and to the PBS buffer.

resistance to water flow increases as  $r^4$  while the resistance to gas flow increases as  $r^3$  where  $r$  is the pore radius. Using the average pore diameters of 60 and 46 nm before and after PEG coating, respectively, one would predict the coated membranes would have 45% of the original gas permeance and 35% of the original hydraulic permeability. For water flow, this expectation is in agreement with the data to within the accuracy of our measurements. Gas flow, however, is less affected by the PEG coating than expected. We reason that water has high affinity for PEG and thus the coated surface maintains the same no-slip condition as a solid wall. On the other hand, the PEG coating will appear as a highly porous matrix to gas flow than a solid structure would provide.

**Nonfouling Properties of PEG-Modified pSiN Membranes.** To study the ability of NPN-PEG to resist protein adsorption, we examined interactions with the two of the most important and abundant proteins in blood albumin (BSA) and IgG. We compared protein adsorption by NPN-PEG to unmodified NPN but also to the silicon rich common substrates of glass and Si. Substrates were exposed to 1 mg/mL solutions of each protein or PBS control for 2 h at room temperature under humidified conditions to prevent evaporation. After thorough washing in PBS, the physically adsorbed fraction remained for analysis by XPS to examine changes in their surface composition.

Protein molecules contain a large number of carbon-bonded nitrogen atoms, enabling assessment of their adsorption through the qualitative and quantitative analysis of the regional N 1s XPS spectra (Figure 6). N 1s XPS spectra of the NPN and PEG-NPN substrates exposed to the PBS solution contain a large N 1s(-Si) peak at  $\sim 395.5$  eV from the bulk silicon nitride

photoemission and a small N 1s(-C) peak at  $\sim 397.5$  eV from the nitrogen atoms in the PEG coating and from nonspecifically adsorbed small organic molecules. After the exposure to the BSA and IgG, the intensity of the N 1s(-C) peak at  $\sim 397.5$  eV increases in NPN and PEG-NPN samples, indicative of the protein adsorption (Figure 6). Similarly, the glass and silicon substrates treated with PBS buffer show only a trace amount of surface nitrogen atoms, whereas the corresponding chips exposed to BSA and IgG show large N 1s peaks in their XPS spectra (Figure 6). These results show that protein adsorption can be monitored by XPS through the changes in the N 1s peak intensity. In the case of nitrogen containing substrates (e.g., silicon nitride or silicon oxy-nitride), protein adsorption can be monitored by comparing areas of the silicon-bonded and carbon-bonded nitrogen atoms, whose binding energies are separated by  $\sim 2$  eV.

To quantify the amount of adsorbed proteins, regional N 1s and Si 2p XPS spectra of the oxidized silicon, glass, NPN, and PEG-NPN substrates exposed to the BSA and IgG solutions were used to measure the thicknesses of the nonspecifically adsorbed protein layers using eq 1. To calculate the protein layer thickness “ $d$ ” on NPN and PEG-NPN substrates, we used N 1s(-C) 398 eV XPS peaks as a unique protein signal  $I_{A(f)}$  and N 1s(-Si) 396 eV peak as characteristic substrate signals  $I_{B(s)}$  (eq 1, Table S3). In the case of BSA and IgG treated samples, to account for the presence of the carbon-bonded nitrogens in the PEG layer, the total area of the N 1s(-C) 398 eV XPS peak was reduced by the area of this peak in the freshly prepared untreated PEG-NPN samples (Table S4). The thickness of the protein layers on the reference silicon and glass substrates was calculated using N 1s XPS peaks as unique protein signals  $I_{A(f)}$

and Si 2p peaks as characteristic substrate signals  $I_{B(s)}$  (see Table S4 for more details). Peak intensities were measured from the regional scans of the corresponding elements using Casa XPS software and atomic relative sensitivity factors of the specific Kratos Ultra DLD XPS instrumentation. We note that the described XPS-based protein thickness measurements assume that the adsorbed protein films are homogeneous and that in the case of nonhomogeneous protein films of variable height and density (or in the cases of submonolayer adsorptions) eq 1 can only be used to approximately estimate the average film thickness over the analytical area. To examine the homogeneity of the protein films adsorbed on the PEG-NPN membrane, we imaged the pure PEG-NPN substrate and the PEG-NPN chips exposed to the IgG and BSA proteins with the tapping mode atomic force microscopy (AFM) and SEM (Figures S5 and S6). The AFM images (Figure S5) show that both protein coatings have higher average roughness than the clean PEG-NPN substrate (3.98 nm (PEG-NPN BSA) and 3.28 nm (PEG-NPN IgG) vs 1.76 nm (clean PEG-NPN)) and that both protein layers do not feature microscopic inhomogeneous domains with significantly different thicknesses. These observations were also supported by the SEM images of the BSA and IgG exposed PEG-NPN membranes (Figure S6). SEM images did not reveal any significant nonuniform protein patches, suggesting homogeneous protein adsorption.

Figure 7 shows that the measured thickness of the adsorbed proteins is the highest on the high surface energy glass and

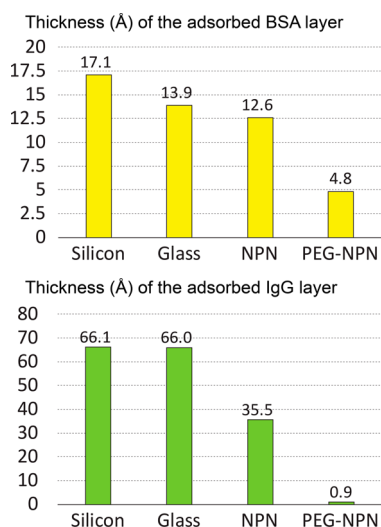


**Figure 7.** Measured thickness of the BSA and IgG protein layers on silicon, glass, NPN, and PEG-NPN.

silicon and that it is lower on the silicon nitride chips. The PEG-functionalized substrates have the thinnest protein layers, confirming that the presented functionalization approach is capable of installing both stable and functional ultrathin coatings on nanoporous materials. PEG-modified substrates adsorbed only submonolayers of the BSA and IgG molecules even after 2 h of exposure, whereas the untreated NPN substrates adsorbed a significantly higher number of protein molecules (260% BSA and 3940% IgG).

## CONCLUSIONS

Our work shows that the vapor-phase carbenylation can be used to form functional, conformal, and stable monolayers of organic molecules on nanoporous substrates without clogging pores. We demonstrated that, due to their overall thinness, these carbenylated coatings do not diminish the excellent transport properties of NPN membranes and shift sieving properties in a predictable fashion. We also demonstrated that, because the functional carbene molecules are attached to the passivated Me-terminated layer via nonhydrolytic Si–C and C–C bonds, they are less prone to hydrolytic cleavage than typical SAMs on oxides and metals. By modifying the carbenylated monolayers with the PEG molecules and by comparing adsorption of the BSA and IgG proteins on the PEG-modified and untreated NPN chips and other substrates, we demonstrated that the combined carbene/PEG functionalization can limit nonspecific protein adsorption despite the ultrathin dimension of the PEG layer. Therefore, the described functionalization method can serve as an alternative technique to the traditional SAM and polymer brush methodologies for applying functional organic coatings on nanoporous materials, which are typically incompatible with molecular self-assembly and can be readily clogged by polymer brushes.

## ASSOCIATED CONTENT

### Supporting Information

The Supporting Information is available free of charge on the ACS Publications website at DOI: [10.1021/acs.chemmater.6b05392](https://doi.org/10.1021/acs.chemmater.6b05392).

Experimental details, characterization methods, and additional data on the thickness and stability measurements (PDF)

## AUTHOR INFORMATION

### Corresponding Authors

\*E-mail: [alexander.shestopalov@rochester.edu](mailto:alexander.shestopalov@rochester.edu).

\*E-mail: [jmcgrath@bme.rochester.edu](mailto:jmcgrath@bme.rochester.edu).

### ORCID

Alexander A. Shestopalov: [0000-0002-5153-7604](https://orcid.org/0000-0002-5153-7604)

### Notes

The authors declare no competing financial interest.

## ACKNOWLEDGMENTS

Financial support of the UR Technology Development Fund, NIH EB021026, and NSF DMR 1228889 is gratefully acknowledged.

## REFERENCES

- Gaborski, T. R.; Snyder, J. L.; Striemer, C. C.; Fang, D. Z.; Hoffman, M.; Fauchet, P. M.; McGrath, J. L. High-Performance Separation of Nanoparticles with Ultrathin Porous Nanocrystalline Silicon Membranes. *ACS Nano* **2010**, *4* (11), 6973–6981.
- Johnson, D. G.; Khire, T. S.; Lyubarskaya, Y. L.; Smith, K. J.; Desormeaux, J. P.; Taylor, J. G.; Gaborski, T. R.; Shestopalov, A. A.; Striemer, C. C.; McGrath, J. L. Ultrathin Silicon Membranes for Wearable Dialysis. *Adv. Chronic Kidney Dis.* **2013**, *20* (6), 508–515.
- Snyder, J. L.; Clark, A.; Fang, D. Z.; Gaborski, T. R.; Striemer, C. C.; Fauchet, P. M.; McGrath, J. L. An Experimental and Theoretical Analysis of Molecular Separations by Diffusion Through Ultrathin Nanoporous Membranes. *J. Membr. Sci.* **2011**, *369* (1–2), 119–129.

- (4) Winans, J.; Smith, K.; Gaborski, T.; Roussie, J.; McGrath, J. Membrane Capacity and Fouling Mechanisms for Ultrathin Nanomembranes in Dead-end filtration. *J. Membr. Sci.* **2016**, *499*, 282–289.
- (5) Mazzocchi, A. R.; Man, A. J.; DesOrmeaux, J. P. S.; Gaborski, T. R. Porous Membranes Promote Endothelial Differentiation of Adipose-Derived Stem Cells and Perivascular Interactions. *Cell. Mol. Bioeng.* **2014**, *7* (3), 369–378.
- (6) Nehilla, B. J.; Nataraj, N.; Gaborski, T. R.; McGrath, J. L. Endothelial Vacuolization Induced by Highly Permeable Silicon Membranes. *Acta Biomater.* **2014**, *10* (11), 4670–4677.
- (7) Getprecharsawas, J.; McGrath, J. L.; Borkholder, D. A. The Electric Field Strength in Orifice-Like Nanopores of Ultrathin Membranes. *Nanotechnology* **2015**, *26* (4), 045704.
- (8) Snyder, J. L.; Getprecharsawas, J.; Fang, D. Z.; Gaborski, T. R.; Striemer, C. C.; Fauchet, P. M.; Borkholder, D. A.; McGrath, J. L. High-Performance, low-voltage electroosmotic pumps with molecularly thin silicon nanomembranes. *Proc. Natl. Acad. Sci. U. S. A.* **2013**, *110* (46), 18425–18430.
- (9) Kavalenka, M. N.; Striemer, C. C.; DesOrmeaux, J. P. S.; McGrath, J. L.; Fauchet, P. M. Chemical Capacitive Sensing Using Ultrathin Flexible Nanoporous Electrodes. *Sens. Actuators, B* **2012**, *162* (1), 22–26.
- (10) DesOrmeaux, J. P. S.; Winans, J. D.; Wayson, S. E.; Gaborski, T. R.; Khire, T. S.; Striemer, C. C.; McGrath, J. L. Nanoporous Silicon Nitride Membranes Fabricated from Porous Nanocrystalline Silicon Templates. *Nanoscale* **2014**, *6* (18), 10798–10805.
- (11) Striemer, C. C.; Gaborski, T. R.; McGrath, J. L.; Fauchet, P. M. Charge- and Size-Based Separation of Macromolecules Using Ultrathin Silicon Membranes. *Nature* **2007**, *445* (7129), 749–753.
- (12) Quintana, R.; Gosa, M.; Jańczewski, D.; Kutnyanszky, E.; Vancso, G. J. Enhanced Stability of Low Fouling Zwitterionic Polymer Brushes in Seawater with Diblock Architecture. *Langmuir* **2013**, *29* (34), 10859–10867.
- (13) Chapman, R. G.; Ostuni, E.; Takayama, S.; Holmlin, R. E.; Yan, L.; Whitesides, G. M. Surveying for Surfaces that Resist the Adsorption of Proteins. *J. Am. Chem. Soc.* **2000**, *122* (34), 8303–8304.
- (14) Ostuni, E.; Chapman, R. G.; Holmlin, R. E.; Takayama, S.; Whitesides, G. M. A Survey of Structure–Property Relationships of Surfaces that Resist the Adsorption of Protein. *Langmuir* **2001**, *17* (18), 5605–5620.
- (15) Paripovic, D.; Klok, H. A. Improving the Stability in Aqueous Media of Polymer Brushes Grafted from Silicon Oxide Substrates by Surface-Initiated Atom Transfer Radical Polymerization. *Macromol. Chem. Phys.* **2011**, *212* (9), 950–958.
- (16) Tugulu, S.; Klok, H.-A. Stability and Nonfouling Properties of Poly(poly(ethylene glycol) methacrylate) Brushes under Cell Culture Conditions. *Biomacromolecules* **2008**, *9* (3), 906–912.
- (17) Jain, P.; Baker, G. L.; Bruening, M. L. Applications of Polymer Brushes in Protein Analysis and Purification. *Annu. Rev. Anal. Chem.* **2009**, *2* (1), 387–408.
- (18) Penfold, J.; Thomas, R. K. Probing Surfactant Adsorption at the Solid–Solution Interface by Neutron Reflectometry. In *Interface Science and Technology*; Toyoko, I., Ed.; Elsevier: London, 2007; pp 87–115.
- (19) O'Dwyer, C.; Gay, G.; Viaris de Lesegno, B.; Weiner, J. The Nature of Alkanethiol Self-Assembled Monolayer Adsorption on Sputtered Gold Substrates. *Langmuir* **2004**, *20* (19), 8172–8182.
- (20) Sun, L.; Crooks, R. M. Indirect Visualization of Defect Structures Contained Within Self-Assembled Organomeraptan Monolayers: Combined Use of Electrochemistry and Scanning Tunneling Microscopy. *Langmuir* **1993**, *9* (8), 1951–1954.
- (21) Poirier, G. E. Mechanism of Formation of Au Vacancy Islands in Alkanethiol Monolayers on Au(111). *Langmuir* **1997**, *13* (7), 2019–2026.
- (22) Poirier, G. E. Characterization of Organosulfur Molecular Monolayers on Au(111) using Scanning Tunneling Microscopy. *Chem. Rev.* **1997**, *97* (4), 1117–1128.
- (23) Claridge, S. A.; Liao, W.-S.; Thomas, J. C.; Zhao, Y.; Cao, H. H.; Cheunkar, S.; Serino, A. C.; Andrews, A. M.; Weiss, P. S. From the Bottom Up: Dimensional Control and Characterization in Molecular Monolayers. *Chem. Soc. Rev.* **2013**, *42* (7), 2725–2745.
- (24) Li, X.-M.; Huskens, J.; Reinhoudt, D. N. Reactive Self-Assembled Monolayers on Flat and Nanoparticle Surfaces, and Their Application in Soft and Scanning Probe Lithographic Nanofabrication Technologies. *J. Mater. Chem.* **2004**, *14* (20), 2954–2971.
- (25) Love, J. C.; Estroff, L. A.; Kriebel, J. K.; Nuzzo, R. G.; Whitesides, G. M. Self-Assembled Monolayers of Thiolates on Metals as a Form of Nanotechnology. *Chem. Rev.* **2005**, *105* (4), 1103–1169.
- (26) Smith, R. K.; Lewis, P. A.; Weiss, P. S. Patterning Self-Assembled Monolayers. *Prog. Surf. Sci.* **2004**, *75* (1–2), 1–68.
- (27) Sullivan, T. P.; Huck, W. T. S. Reactions on Monolayers: Organic Synthesis in Two Dimensions. *Eur. J. Org. Chem.* **2003**, *2003*, 17–29.
- (28) Linford, M. R.; Fenter, P.; Eisenberger, P. M.; Chidsey, C. E. D. Alkyl Monolayers on Silicon Prepared from 1-Alkenes and Hydrogen-Terminated Silicon. *J. Am. Chem. Soc.* **1995**, *117* (11), 3145–3155.
- (29) Sieval, A. B.; Demirel, A. L.; Nissink, J. W. M.; Linford, M. R.; van der Maas, J. H.; de Jeu, W. H.; Zuilhof, H.; Sudhölter, E. J. R. Highly Stable Si–C Linked Functionalized Monolayers on the Silicon (100) Surface. *Langmuir* **1998**, *14* (7), 1759–1768.
- (30) Shestopalov, A. A.; Clark, R. L.; Toone, E. J. Catalytic Microcontact Printing on Chemically Functionalized H-Terminated Silicon. *Langmuir* **2010**, *26* (3), 1449–1451.
- (31) Wang, X.; Ruther, R. E.; Streifer, J. A.; Hamers, R. J. UV-Induced Grafting of Alkenes to Silicon Surfaces: Photoemission versus Excitons. *J. Am. Chem. Soc.* **2010**, *132* (12), 4048–4049.
- (32) Cicero, R. L.; Linford, M. R.; Chidsey, C. E. D. Photoreactivity of Unsaturated Compounds with Hydrogen-Terminated Silicon(111). *Langmuir* **2000**, *16* (13), 5688–5695.
- (33) Terry, J.; Mo, R.; Wigren, C.; Cao, R.; Mount, G.; Pianetta, P.; Linford, M. R.; Chidsey, C. E. D. Reactivity of the HSi(1 1 1) surface. *Nucl. Instrum. Methods Phys. Res., Sect. B* **1997**, *133* (1), 94–101.
- (34) Holland, J. M.; Stewart, M. P.; Allen, M. J.; Buriak, J. M. Metal Mediated Reactions on Porous Silicon Surfaces. *J. Solid State Chem.* **1999**, *147* (1), 251–258.
- (35) Hurley, P. T.; Nemanick, E. J.; Brunschwig, B. S.; Lewis, N. S. Covalent Attachment of Acetylene and Methylacetylene Functionality to Si(111) Surfaces: Scaffolds for Organic Surface Functionalization while Retaining Si–C Passivation of Si(111) Surface Sites. *J. Am. Chem. Soc.* **2006**, *128* (31), 9990–9991.
- (36) Juang, A.; Scherman, O. A.; Grubbs, R. H.; Lewis, N. S. Formation of Covalently Attached Polymer Overlayers on Si(111) Surfaces Using Ring-Opening Metathesis Polymerization Methods. *Langmuir* **2001**, *17* (5), 1321–1323.
- (37) Allongue, P.; de Villeneuve, C. H.; Pinson, J.; Ozanam, F.; Chazalviel, J. N.; Wallart, X. Organic Monolayers on Si(111) by Electrochemical Method. *Electrochim. Acta* **1998**, *43* (19–20), 2791–2798.
- (38) de Villeneuve, C. H.; Pinson, J.; Bernard, M. C.; Allongue, P. Electrochemical Formation of Close-Packed Phenyl Layers on Si(111). *J. Phys. Chem. B* **1997**, *101* (14), 2415–2420.
- (39) Robins, E. G.; Stewart, M. P.; Buriak, J. M. Anodic and Cathodic Electrografting of Alkynes on Porous Silicon. *Chem. Commun.* **1999**, *24*, 2479–2480.
- (40) Niederhauser, T. L.; Jiang, G.; Lua, Y.-Y.; Dorff, M. J.; Woolley, A. T.; Asplund, M. C.; Berges, D. A.; Linford, M. R. A New Method of Preparing Monolayers on Silicon and Patterning Silicon Surfaces by Scribing in the Presence of Reactive Species. *Langmuir* **2001**, *17* (19), 5889–5900.
- (41) Yang, L.; Lua, Y.-Y.; Lee, M. V.; Linford, M. R. Chemo-mechanical Functionalization and Patterning of Silicon. *Acc. Chem. Res.* **2005**, *38* (12), 933–942.
- (42) Leroux, Y. R.; Fei, H.; Noël, J.-M.; Roux, C.; Hapiot, P. Efficient Covalent Modification of a Carbon Surface: Use of a Silyl Protecting Group To Form an Active Monolayer. *J. Am. Chem. Soc.* **2010**, *132* (40), 14039–14041.
- (43) Yang, W.; Auciello, O.; Butler, J. E.; Cai, W.; Carlisle, J. A.; Gerbi, J. E.; Gruen, D. M.; Knickerbocker, T.; Lasseter, T. L.; Russell,

J. N.; Smith, L. M.; Hamers, R. J. DNA-Modified Nanocrystalline Diamond Thin-Films as Stable, Biologically Active Substrates. *Nat. Mater.* **2002**, *1* (4), 253–257.

(44) Stavis, C.; Clare, T. L.; Butler, J. E.; Radadia, A. D.; Carr, R.; Zeng, H.; King, W. P.; Carlisle, J. A.; Aksimentiev, A.; Bashir, R.; Hamers, R. J. Surface Functionalization of Thin-Film Diamond for Highly Stable and Selective Biological Interfaces. *Proc. Natl. Acad. Sci. U. S. A.* **2011**, *108* (3), 983–988.

(45) Li, X.; Ma, W.; Shestopalov, A. A. Vapor-Phase Carbenylation of Hard and Soft Material Interfaces. *Langmuir* **2016**, *32* (44), 11386–11394.

(46) Powell, C. J.; Jablonski, A. *NIST Electron Effective-Attenuation-Length Database*; National Institute of Standards and Technology: Gaithersburg, MD, 2011; Vol. Version 1.3.

(47) Seah, M. P. Quantification of AES and XPS. In *Practical Surface Analysis by Auger and X-ray Photoelectron Spectroscopy*; Briggs, D., Seah, M. P., Eds.; John Wiley and Sons: New York, 1983; Chapter 5, p 211.

(48) Seah, M. P.; Spencer, S. J. Ultrathin SiO<sub>2</sub> on Si. II. Issues in Quantification of the Oxide Thickness. *Surf. Interface Anal.* **2002**, *33* (8), 640–652.

(49) Hesse, R.; Streubel, P.; Szargan, R. Improved Accuracy of Quantitative XPS Analysis Using Predetermined Spectrometer Transmission Functions with UNIFIT 2004. *Surf. Interface Anal.* **2005**, *37* (7), 589–607.

(50) Tielsch, B. J.; Fulghum, J. E. Differential Charging in XPS. Part III. A Comparison of Charging in Thin Polymer Overlayers on Conducting and Non-Conducting Substrates. *Surf. Interface Anal.* **1997**, *25* (11), 904–912.

(51) Jones, J. A.; Qin, L. A.; Meyerson, H.; Kwon, I. I. K.; Matsuda, T.; Anderson, J. M. Instability of Self-Assembled Monolayers (SAM) as a Model Material System for Macrophage/FBGC Cellular Behavior. *J. Biomed. Mater. Res., Part A* **2008**, *86A* (1), 261–268.

(52) More, S.; Graaf, H.; Nonogaki, Y.; Urisu, T. Influence of substrate roughness on the formation of self-assembled monolayers (SAM) on Silicon [100]; Digest of Papers. Microprocesses and Nanotechnology 2001; In *2001 International Microprocesses and Nanotechnology Conference* (IEEE Cat. No.01EX468), Oct. 31 to Nov. 2, 2001; pp 178–179.

(53) Zhu, M.; Lerum, M. Z.; Chen, W. How to Prepare Reproducible, Homogeneous, and Hydrolytically Stable Aminosilane-derived Layers on Silica. *Langmuir* **2012**, *28* (1), 416–423.